A one-way coupled, Euler–Lagrangian simulation of bubble coalescence in a turbulent pipe flow

M.D. Mattson, K. Mahesh *

University of Minnesota, Aerospace Engineering & Mechanics, 107 Akerman Hall, 110 Union Street, Minneapolis, MN 55455-0153, USA

ARTICLE INFO

ABSTRACT

A bubble coalescence model is developed using an Euler–Lagrangian approach for unstructured grids. The Eulerian carrier fluid is solved using large-eddy simulation (LES) and the Lagrangian particle motion is solved with equations relating the turbulent motion of the carrier fluid to forces on each discrete bubble. The collision process is deterministic; bubble–bubble collisions are assumed to be binary and are modeled using a hard-sphere approach. A stochastic approach is used to model coalescence, with the probability of coalescence being a function of the bubble–bubble interaction timescale and the time to drain fluid between the colliding bubbles. The intention is to develop and validate the collision and coalescence model, neglecting two-way coupling turbulent subgrid stress transport of bubbles and the modification of the subgrid stress by the bubbles. Coalescence in a bubbly, turbulent pipe flow in microgravity is simulated with conditions similar to experiments by Colin et al. (Colin, C., Fabre, J., Dukler, A.E., 1991. Gas–liquid flow at microgravity conditions – I. Dispersed bubble and slug flow. Int. J. Multiphase Flow 17 (4), 533–544.) and excellent agreement of bubble size distribution is obtained between simulation and experiment. With increasing downstream distance, the number density of bubbles decreases due to coalescence and the average probability of coalescence decreases slightly due to an increase in overall bubble size.

1. Introduction

Bubbly flows are important for a wide range of practical applications. For example, the formation and behavior of bubbles is critical in many heat transfer problems where liquid water contacting a hot surface boils and the resulting vapor bubbles move heat away from the hot surface through phase change of the liquid and buoyancy-driven bubble motion. Bubbles are also frequently observed in marine flows. The presence of bubbles drastically modifies the speed of sound in the bubbly mixture, which has implications for marine acoustic signatures and detection (Trevorrow et al., 1994). The behavior of these flows depends on the size distribution of the bubbles and void fraction profiles. The physical phenomena observed in bubbly flows are rich and complex, and include bubble surface deformation, growth and collapse, collisions with other bubbles and surfaces, coalescence and breakup. The challenge is to develop robust, yet efficient and practical, numerical models of the complicated bubble physics to accurately predict these flows in full-scale applications.

A large amount of work has been performed to develop numerical approaches for simulating unsteady bubbly flow while accounting for the effect of bubble coalescence (Olmos et al., 2001; Sommerfeld et al., 2003; Chen et al., 2005; van den Hengel et al., 2005; Darmana et al., 2006; Bokkers et al., 2006). Most work uses either an Euler-Euler (two-fluid approach) or an Euler–Lagrangian approach, where the dispersed phase is modeled by Lagrangian particles. In the Euler-Euler approach, bubbles are not tracked individually but treated as a continuum and various closures for interaction of the bubble phase and the carrier phase along with stochastic models for bubble–bubble collisions and coalescence must be included. For example, the work of Olmos et al. (2001) coupled an Euler–Euler approach along with population balance equations to model the evolution of bubble size. A coalescence model by Prince and Blanch (1990) was used, with a $k - \epsilon$ turbulence model for the liquid phase. This coalescence model assumes isotropic turbulence in its determination of bubble–bubble collisions. Chen et al. (2005) performed Euler–Euler simulations using a bubble population balance equations and compared a variety of bubble breakup and coalescence models. The carrier-phase flow was also simulated with a $k - \epsilon$ turbulence model.

An advantage of Euler–Lagrangian approaches is that the locations and velocities of each individual are explicitly known and bubble–bubble collisions can be computed directly. Darmana et al. (2006) developed a coalescence model using the film-drainage timescale by Prince and Blanch (1990) and the bubble–bubble

* Corresponding author. Tel.: +1 612 624 4175.
  E-mail address: mahesh@aem.umn.edu (K. Mahesh).

interaction timescale by Sommerfeld et al. (2003). Bokkers et al. (2006) performed Euler–Lagrangian simulations with a hard-sphere collision model, assuming all collisions led to coalescence (until a maximum bubble size was reached).

Additionally, there has been much work on bubble–bubble and particle–particle collisions. Early simulations by Sangani and Didwania (1993) performed inviscid simulations of bubbles rising in a liquid, including binary bubble–bubble collisions and observed aggregation of bubbles in planes transverse to gravity. Sundaram and Collins (1997) performed Euler–Lagrangian simulations of heavy point-particles suspended in isotropic turbulence and found that particle inertia (parameterized by Stokes number St) affected particle collision frequency and particle concentration. At low St, the collision frequency increased with St due to increased particle concentration in low-vorticity regions of the flow and an increase in particle–particle relative velocity. The collision frequency continued to increase up to St $\approx$ 4, then decreased due to de-correlation of the particle–particle velocities. When solving particle motion from LES of the carrier-phase equations, neglecting the influence of subgrid scale fluctuations has been shown to affect the preferential concentration of inertial particles (Fede and Simonin, 2006; Pozorski and Apte, 2009), thus reducing the collision frequency (Wang et al., 2009). This effect is pronounced for particles of low Stokes numbers (Jin et al., 2010). Neglecting the influence of subgrid scales is likely to affect bubble–bubble preferential concentration and collision frequency, though we ignore them in this work. Our contribution is threefold: (i) propose a point-particle coalescence model (ii) provide validation with respect to the microgravity experiment of Colin et al. (1991) and (iii) study details of the bubble–bubble collisions and coalescence provided by our model.

The objective of this paper is to perform high Reynolds number simulations of bubbly flow and account for bubble coalescence without resorting to Reynolds-Averaged Navier–Stokes (RANS) turbulence models or stochastic approximations for bubble–bubble collisions. In flows with complex geometries, models of the collision and coalescence process assuming isotropy of the turbulence (such as Prince and Blanch, 1990) will not be accurate in general, due to the non-equilibrium influence of geometry on the turbulence. An Euler–Lagrangian methodology is used, and bubble–bubble collisions are computed directly using a hard-sphere approach. The bubble coalescence model of Kamp et al. (2001) is extended to unsteady flows where bubble–bubble collisions and the relative velocity between colliding bubbles are computed directly.

The paper is organized as follows: first, the details of the numerical approach are described (Sections 2 and 3). The description of the collision (Section 4) and coalescence models (Section 5) are then discussed. The coalescence model is validated through comparison to experimental results of Colin et al. (1991). Details of the simulation parameters are provided in Section 6. The results of the carrier phase turbulent statistics, bubble size distribution and collision details are then described in Sections 7 and 8. Physical details of the collision and coalescence process are then discussed in Section 9.

2. Numerical method

A point-particle, one-way coupled Euler–Lagrangian method is used to model the bubble convection and a hard-sphere model is used for bubble collisions. For simplicity, finite-size effects of the bubble on the surrounding flow are ignored. In this approach, the bubbles are modeled as a dispersed phase, with individual bubbles treated as point-particles governed by an equation for bubble motion, combined with a continuous carrier phase described by the Navier–Stokes equations. Thus, for simplicity, hydrodynamic forces

on bubbles that are larger than the grid spacing (as occasionally observed in the considered cases) are computed directly from the forces obtained from the bubble center; no attempt is made to correct for the finite size of the bubble. A finite-volume approach (Mahesh et al., 2004) is used to solve the Navier–Stokes equations for the carrier phase. The resolved velocity field is solved using LES, with the subgrid stress modeled using the dynamic Smagorinsky model proposed by Germano et al. (1991) and Lilly (1992) as described in Mahesh et al. (2004). A constant density of the carrier phase is assumed and the incompressible Navier–Stokes equations are solved using a predictor–corrector approach. Also, the carrier phase solver discretely conserves kinetic energy, ensuring robustness at high Reynolds numbers. Each bubble is tracked individually and characterized by its instantaneous position ($\vec{Y}$), velocity ($\vec{v}$) and size (bubble radius R). This method has been developed to simulate large numbers of bubbles and previously applied to problems without accounting for bubble–bubble collisions or coalescence (Mattson and Mahesh, 2011).

The motion of each individual bubble is modeled by the equation (Johnson et al., 1966; Thomas et al., 1984; Auton et al., 1988; Mattson and Mahesh, 2011)

$$\frac{d\vec{v}}{dt} = -2\vec{g} + 3\frac{D\vec{u}}{Dt} + \frac{3}{4}\frac{C_D}{R}|\vec{u} - \vec{v}|(\vec{u} - \vec{v}) + 2C_L(\vec{u} - \vec{v}) \times \vec{\omega}. \qquad (1)$$

The four terms on the right-hand side denote the (i) buoyancy, (ii) fluid-acceleration, (iii) drag and (iv) lift terms, respectively, with $\vec{g}$ the gravitational vector, $\vec{u}$ the Eulerian fluid velocity and $\vec{\omega}$ the fluid vorticity at the bubble location. For the microgravity simulation described in this paper, the buoyancy term was set to zero.

The expression for the coefficient of bubble drag (C_D), determined experimentally by Haberman and Morton (1953) as function of bubble Reynolds number, is obtained from

$$C_D = \frac{24}{Re_b}\left(1.0 + 0.197Re_b^{0.63} + 2.6 \times 10^{-4}Re_b^{1.38}\right), \qquad (2)$$

where the bubble Reynolds number is defined as $Re_b = 2R|\vec{u} - \vec{v}|/\nu_f$, where ν_f is the fluid kinematic viscosity. For small bubbles in water, the drag profile is similar to that of solid spheres ($C_D \sim 24/Re_b$), due to the contamination by surfactants of the bubble surface.

Auton et al. (1988) showed that the constant lift coefficient of 1/2 is appropriate in the inviscid limit and that in the added mass and fluid acceleration forces the material derivative of the fluid velocity is the appropriate term for the fluid acceleration. A constant lift coefficient, C_L, of 1/2 and a constant added-mass coefficient, C_M, of 1/2 for a sphere are used (Auton, 1987; Batchelor, 1967). Although in the inviscid limit, a lift coefficient of 1/2 is not controversial, at moderate Reynolds numbers the value of the lift coefficient has not been conclusively determined. Sridhar and Katz (1995) performed experiments at bubble Reynolds numbers between 20 and 80 and found lift coefficients larger than the inviscid result which also depended on the local vorticity. Legendre and Magnaudet (1998) performed numerical simulations of flow over a sphere in weak shear Sr $\leqslant$ 1, with Sr defined as the velocity difference across the bubble divided by the relative velocity between the bubble and the carrier fluid, and found lift coefficients that were between 1 and 0.5 for $Re_b > 1$, depending on local vorticity. The lift coefficient approached 1/2 as the Reynolds number increased. The bubble Reynolds number in this work is ~100–1000 and the maximum shear parameter $Sr_{max} \sim 0.1$ near the wall, so using a lift coefficient of 1/2 is reasonable.

This approach can simulate flows with large numbers of bubbles in complex geometries over a wide range of Reynolds numbers. Bubble-wall interactions are treated as hard-sphere, inelastic collisions and bubble–bubble interactions are computed as binary, hard-sphere collisions. The following sections describe the collision and coalescence models developed for the Euler–Lagrangian approach.

3. Bubble time integration

The bubble position and velocity over time is determined by integrating the bubble acceleration equation (Eq. (1)). This is done with a hybrid explicit–implicit approach. The simulation is divided into two different timescales: the Eulerian fluid timestep Δt and the path integration timestep of the bubbles Δt_{bub}, where $\Delta t = t_2 - t_1$ and $\Delta t_{bub} = t^{k+1} - t^k$ (see Fig. 1). The Eulerian fluid variables are known at $t = t_1$ and $t = t_2$ from the advancement of the Navier–Stokes equations.

The Eulerian values in Eq. (1) must be evaluated at time $t = t^k$ and at the bubble position $\vec{x} = \vec{Y}^k$ on unstructured grids. A linear interpolation approach was chosen for ease of implementation for unstructured grids. Many higher-order interpolation schemes (such as that used by Elghobashi and Truesdell (1992)), though more accurate, are not straight-forward to implement for a general, unstructured mesh. For complex geometries, highly skewed mesh elements are unavoidable and a robust interpolation scheme is required. Apte et al. (2003) found first-order interpolation of the Eulerian velocity field to be sufficient in resolving the particle motions.

Spatial gradients of the carrier-phase parameters at the control volume centroids are obtained using a linear least-squares method. The fluid velocity at the bubble location $\vec{u}|_{x=Y^k}$ is interpolated from the values at the control volume centroid by

$$\vec{u}(t^k)\big|_{\vec{x}=\overrightarrow{Y^k}} = \vec{u}(t^k)\big|_{\vec{x}_{cv}} + \left[\left(\overrightarrow{Y^k} - \vec{x}_{cv}\right)\cdot\vec{\nabla}\right]\vec{u}(t^k)\big|_{\vec{x}_{cv}} \tag{3}$$

The spatial gradients $\partial u_i/\partial x_j$ are determined at the control volume centroids using a least-squares approach. To obtain the control volume values of velocity required in Eq. (3) at time $t = t^k$, a linear time interpolation is performed using

$$u_i(t^k)\big|_{\vec{x}_{cv}} = \frac{1}{\Delta t}\left[(t^k - t_1)u_i(t_2)\big|_{\vec{x}_{cv}} + (t_2 - t^k)u_i(t_1)\big|_{\vec{x}_{cv}}\right]. \tag{4}$$

It is assumed that time derivatives between t_2 and t_1 are constant and that spatial gradients are constant within the control volume. The vorticity vector at any point inside a control volume is then

$$\vec{\omega}\big|^k_{\vec{x}=\overrightarrow{Y^k}} = \vec{\omega}\big|_{\vec{x}_{cv}}^k = \vec{\nabla}\times\vec{u}\big|^k_{\vec{x}_{cv}}. \tag{5}$$

The fluid material derivative at the bubble location at time $t = t^k$ is is obtained from

$$\frac{Du_i}{Dt}\bigg|^k_{\vec{x}=\overrightarrow{Y^k}} = \left(\frac{\partial u_i}{\partial t} + u_j\frac{\partial u_i}{\partial x_j}\right)\bigg|^k_{\vec{x}=\overrightarrow{Y^k}}. \tag{6}$$

All values must be interpolated in time to $t = t^k$ and in space to the bubble location $\vec{x} = \overrightarrow{Y^k}$. The unsteady fluid-velocity term is obtained from

$$\frac{\partial u_i}{\partial t}\bigg|^k_{\vec{x}=\overrightarrow{Y^k}} = \frac{\partial u_i}{\partial t}\bigg|^k_{\vec{x}_{cv}} + L_j^k\frac{\partial}{\partial x_j}\left(\frac{\partial u_i}{\partial t}\right)\bigg|^k_{\vec{x}_{cv}}, \tag{7}$$

where the distance vector $\overrightarrow{L}$ is equal to the distance from the bubble position to the centroid, $\overrightarrow{L} = \overrightarrow{Y} - \vec{x}_{cv}$. Assuming that the spatial gradients within a control volume are constant,

$$\frac{\partial u_i}{\partial x_j}\bigg|^k_{\vec{x}=\overrightarrow{Y^k}} = \frac{\partial u_i}{\partial x_j}\bigg|^k_{\vec{x}_{cv}}, \tag{8}$$

and the convective term can be written as

$$\left(u_j\frac{\partial u_i}{\partial x_j}\right)\bigg|^k_{\vec{x}=\overrightarrow{Y^k}} = (u_j)\big|^k_{\vec{x}=\overrightarrow{Y^k}}\left(\frac{\partial u_i}{\partial x_j}\right)\bigg|^k_{\vec{x}_{cv}}. \tag{9}$$

The bubble velocity at time $t = t^{k+1}$ is integrated using the Adams–Bashforth approach:

$$v_i^{k+1} = v_i^k + \Delta t_{bub}\left(\frac{3}{2}\frac{dv_i^k}{dt} - \frac{1}{2}\frac{dv_i^{k-1}}{dt}\right). \tag{10}$$

Once the bubble velocity has been integrated to $t = t^{k+1}$, the bubble position is integrated using the trapezoidal method:

$$Y_i^{k+1} = Y_i^k + \frac{\Delta t_{bub}}{2}\left(v_i^{k+1} + v_i^k\right). \tag{11}$$

The bubble equations are advanced from k, $k + 1$, $k + 2$, etc. until $t = t_2$ is reached. Then the fluid equations are updated by Δt and the bubble integration process begins anew.

4. Collision model

A collision model assuming binary, hard-sphere collisions (Allen and Tildesley, 1988) is used. The timestep Δt_{bub} is the timescale the bubbles will be advanced if no collisions occur (see Fig. 1). The time it takes for bubble m to collide with bubble n is defined as $t_{m,n}$. At the moment of collision, bubbles m and n are assumed to be touching, with zero distance between them. For bubbles with a constant radius and assuming constant bubble velocities between collisions, the equation for position at the moment of collision is

$$|\vec{r}_{m,n}(t + t_{m,n})| = |\vec{r}_{m,n}(t) - \vec{v}_{m,n}t_{m,n}| = R_m + R_n, \tag{12}$$

where the relative position $\vec{r}$ of bubble n from m is $\vec{r}_{m,n} = \overrightarrow{Y}_n - \overrightarrow{Y}_m$ and the relative velocity between the two bubbles m and n (in the frame of reference of bubble m) is defined as $\vec{v}_{m,n} = \vec{v}_n - \vec{v}_m$.

Fig. 2 is a schematic of a binary collision between bubbles m and n. The variable $b_{m,n}$ is defined by $b_{m,n} = \vec{r}_{m,n}\cdot\vec{v}_{m,n}$. Collision will only occur between bubbles m and n if $b_{m,n} < 0$, since if $\vec{r}_{m,n}\cdot\vec{v}_{m,n} > 0$, the bubbles are moving away from each other. The collision angle θ_c is obtained from

$$\theta_c = \cos^{-1}\left[\frac{\vec{r}_{m,n}\cdot\vec{v}_{m,n}}{|\vec{r}_{m,n}||\vec{v}_{m,n}|}\right].$$

At the moment of collision, the two bubbles are touching and therefore

$$|\vec{r}_{m,n}|^2 + 2b_{m,n}t_{m,n} + |\vec{v}_{m,n}|^2t_{m,n}^2 - (R_m + R_n)^2 = 0. \tag{13}$$

The time to collision is obtained from the smallest real solution of Eq. (13) for $t_{m,n}$. The integration of the bubble position over Δt is performed as follows, starting from $t^k = t_1$:
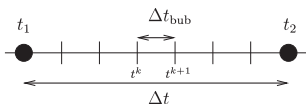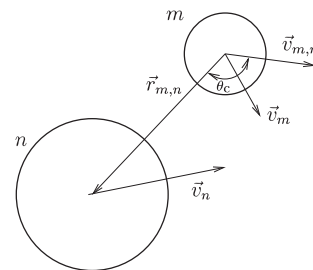

Fig. 1. Discretization of fluid timestep Δt and bubble timestep Δt_{bub} from time t_1 to t_2.

Fig. 2. Schematic of parameters of collision between bubble m and bubble n.

(a) Looping over all particles, find collision partners by determining the minimum $t_{m,n}$ for each bubble pair.
(b) Determine the minimum collision time t_{col} by finding the minimum $t_{m,n}$ over all collision pairs.
if $t_{col} < \Delta t_{bub}$
 (c) Advance all bubbles by t_{col} and apply collision dynamics to the collision pair.
 (d) Update collision partners of the bubbles that have just collided.
else
(c) Advance all bubbles by Δt_{bub}.
if $t > t_2$
Go back to (a).
else
Go back to (b).

This loop is performed until all bubbles have been integrated to t^{k+1}. The process is repeated until $t^{k+1} = t_2$, after which the Eulerian fluid equations are advanced and all bubble collision partners are recalculated. Then the bubble position integration process begins anew.

5. Coalescence model

When two bubbles collide, a thin liquid film is sandwiched between them. The energy of collision leads to deformation of the bubble surface and the subsequent separation of the bubbles. Surface tension effects drain the liquid film and coalescence occurs if the bubbles have not separated before the film ruptures. The likelihood of coalescence is a function of two timescales: the film drainage timescale t_d and the bubble–bubble interaction timescale t_i (Chesters, 1991; Chesters and Hofman, 1982).

Kamp et al. (2001) derived a coalescence model with the assumption of large Reynolds numbers and that bubble–bubble collisions are driven by turbulent fluctuations (ignoring mean gradients in the flow and buoyant effects). The turbulent flow and bubble velocities were modeled using a RANS approach. However, RANS methodologies are generally not accurate when simulating separated flow or particle transport, due to regions of anisotropy in the turbulent fluctuations and the fact that path lines integrated on a mean field are inherently different than mean paths obtained from instantaneous path lines. Additionally, the eddy viscosity assumption itself can also be invalid (Muppidi and Mahesh, 2008). To predict particle or bubble transport, it is important to have realistic velocity fields along particle/bubble trajectories. With large-eddy simulation (LES), the large scales of the flow that contain a majority of the kinetic energy are resolved which increases the accuracy of the Lagrangian dispersion.

A method for determining the probability of coalescence at the moment of collision was developed using an Euler–Lagrangian formulation. The probability of coalescence is determined stochastically, as in Kamp et al. (2001), with the probability of coalescence computed from a ratio of coalescence timescales. However, in the Euler–Lagrangian approach, the bubble velocities are directly determined from the instantaneous Eulerian flow field obtained by LES and bubble–bubble collisions are computed for each bubble as discrete, instantaneous events.

5.1. Conservation of kinetic energy

The basic idea behind the coalescence model is as follows (please see Kamp et al. (2001) for more details). Consider two spheres with radii R_m and R_n approaching each other along their line of centers with velocities U_m and U_n. The velocities U_m and U_n are obtained from the component of the bubble velocities along the collision line-of-centers. The unit normal vector $\hat{n}_{m,n}$ pointing

from bubble m to n is given by $\hat{n}_{m,n} = \vec{r}_{m,n}/|\vec{r}_{m,n}|$. The velocities normal and tangential to the line of centers are then

$$U_m = v_{m,N} = \vec{v}_m \cdot \hat{n}_{m,n}, \quad \vec{v}_{m,T} = \vec{v}_m - v_{m,N}\hat{n}_{m,n}$$
$$U_n = v_{n,N} = \vec{v}_n \cdot \hat{n}_{m,n}, \quad \vec{v}_{n,T} = \vec{v}_n - v_{n,N}\hat{n}_{m,n}$$

For surfactant-free surfaces, the shear stress at the bubble surface is zero, and a potential flow can be used to describe the flow field, in the limit of large Reynolds numbers. The kinetic energy due to the motion of the two spheres can then be expressed (Lamb, 1945) by

$$E_k = \frac{1}{2}\left(LU_m^2 - 2MU_mU_n + NU_n^2\right), \tag{14}$$

with the coefficients L, M and N determined by

$$L = \frac{2}{3}\pi\rho_f R_m^3\left(1 + \frac{3R_m^3 R_n^3}{l^3 f_1^3} + \frac{3R_m^6 R_n^6}{l^3 f_1^3(l - f_2)^3 f_3^3} + \cdots\right), \tag{15}$$

$$M = 2\pi\rho_f \frac{R_m^3 R_n^3}{l^3}\left(1 + \frac{R_m^3 R_n^3}{g_1^3(l - g_2)^3} + \frac{R_m^6 R_n^6}{g_1^3 g_3^3(l - g_2)^3(l - g_4)^3} + \cdots\right), \tag{16}$$

$$N = \frac{2}{3}\pi\rho_f R_n^3\left(1 + \frac{3R_m^3 R_n^3}{l^3 g_1^3} + \frac{3R_m^6 R_n^6}{l^3 g_1^3(l - g_2)^3 g_3^3} + \cdots\right), \tag{17}$$

where

$$f_1 = l - R_n^2/l, \quad f_2 = R_m^2/f_1, \quad f_3 = l - R_n^2/(l - f_2), \quad f_4 = R_m^2/f_3, \tag{18}$$

$$g_1 = l - R_m^2/l, \quad g_2 = R_n^2/g_1, \quad g_3 = l - R_m^2/(l - g_2), \quad g_4 = R_n^2/g_3, \tag{19}$$

and $l = |\vec{Y}_n - \vec{Y}_m|$.

It is clear from these expressions that as two particles approach each other, their respective velocities will change to conserve the total kinetic energy. As the two bubbles approach each other, the coefficients $L \to L_0$, $M \to M_0$ and $N \to N_0$ as $l \to R_m + R_n$. The terms $m_m = L_0 - M_0$ and $m_n = N_0 - M_0$ are defined to obtain a composite average velocity $U_0 = (m_mU_m + m_nU_n)/(m_m + m_n)$ and relative velocity $V = U_m - U_n$. The kinetic energy that is relevant to coalescence is due to the energy associated with the relative velocity

$$(E_k)_{coalescence} = C_{vm}\left(\frac{\pi\rho_f}{6}\right)d_{eq}^3\left(\frac{V}{2}\right)^2, \tag{20}$$

where C_{vm} is an added mass coefficient defined as

$$C_{vm} = \frac{12}{\pi\rho_f d_{eq}^3}\frac{L_0 N_0 - M_0^2}{L_0 - 2M_0 + N_0}, \tag{21}$$

where d_{eq} is the "equivalent" diameter defined as

$$d_{eq} = \frac{2d_m d_n}{d_m + d_n}, \tag{22}$$

where the bubble diameter is twice the bubble radius (e.g. $d_m = 2R_m$) for spherical bubbles.

5.2. Bubble coalescence timescales

A formulation for the ratio of the bubble coalescence timescales, derived by Kamp et al. (2001) for finite collision Weber numbers, is

$$\frac{t_d}{t_i} = \frac{k_1}{2\pi}\sqrt{\frac{3\rho_f V_0^2 d_{eq}}{C_{vm}\sigma}}, \tag{23}$$

where V_0 is the bubble–bubble relative velocity at the moment of collision. The experimentally determined coefficient k_1 was found to be equal to 2.5 when comparing to experimental results Duine-veld (1994) of a single bubble coalescing with a free surface. The theoretical coalescence probability of two bubbles traveling along their line of centers is then obtained from

$$P_c = \begin{cases} 0 & \text{if } t_d > t_i \\ 1 & \text{if } t_d \leqslant t_i. \end{cases} \qquad (24)$$

In practice, the collisions will not always be along line of centers and a smooth, semi-empirical function (Coulaloglou and Tavla-rides, 1977) is used to describe the coalescence probability

$$P_c \approx \exp\left(-\frac{t_d}{t_i}\right). \qquad (25)$$

Once a collision has been determined to occur, the coalescence probability is calculated and a random number x_{ran} (uniformly distributed from [0–1]) is generated. Whether or not coalescence has occurred for each collision is then obtained from

If $(x_{\text{ran}} < P_c) \quad \rightarrow \quad$ coalescence occurs
Else $\qquad\qquad \rightarrow \quad$ coalescence does not occur.

The coalescence model is used only with respect to determining the probability of coalescence; the bubble equation of motion and the potential-flow relation for the coalescence model are de-coupled. Viscous effects, though not explicitly accounted for in the theoretical derivation, can in theory be obtained from the coefficient k_1. As applied to the turbulent pipe problem, viscous effects are likely to be small since the mean bubble Reynolds number (determined by the relative bubble–bubble velocity V, bubble diameter d and kinematic viscosity ν_f of the continuous phase) is large (≈ 750, see Fig. 16).

5.3. Bubble-wall collisions

The bubble-wall collisions are treated as frictionless, specular collisions. The bubble velocity after collision is obtained from

$$\vec{v} = \vec{v}_0 + 2|\vec{v}_0 \cdot \hat{n}|\hat{n}, \qquad (26)$$

where $\hat{n}$ is the inward-pointing wall normal and $\vec{v}_0$ is the bubble velocity before collision.

5.4. Bubble–bubble collision, no coalescence

If it has been determined that the bubbles will collide but not coalesce, an instantaneous hard-sphere collision is assumed to have occurred (assuming that t_i is very small). With this assumption, the normal velocity after collision becomes $V = -V_0$ from conservation of kinetic energy. In the case of two bubbles moving along line of centers in a potential flow, this velocity would increase as the two bubbles move apart. However, we assume that the external forces on the bubble due to the surrounding turbulent flow has a greater affect on bubble motion than the change in the effective coefficient of added mass. The bubble velocities immediately after collision are then

$$v_{m,N} = U_0 - \frac{N_0 - M_0}{L_0 - 2M_0 + N_0}V_0, \quad v_{n,N} = U_0 + \frac{L_0 - M_0}{L_0 - 2M_0 + N_0}V_0$$

and

$$\vec{v}_m = \vec{v}_{m,T} + v_{m,N}\hat{n}_{m,n}, \quad \vec{v}_n = \vec{v}_{n,T} + v_{n,N}\hat{n}_{m,n}.$$

5.5. Bubble–bubble collision, with coalescence

If the binary collision results in coalescence, the two bubbles merge into one. Once this has been determined to happen, the

parameters of the resulting bubble must be determined. The "new" bubble is now defined with superscript "*." The resulting bubble radius is obtained from mass conservation to be

$$R^* = \left(R_m^3 + R_n^3\right)^{1/3}. \qquad (27)$$

The total momentum is conserved from before and after coalescence. The bubble and the surrounding fluid around a bubble have momentum that is proportional to the bubble volume and velocity. Assuming that the momentum when the two bubbles are far apart is equal to the momentum when the two bubbles coalesce, the expression for the new bubble velocity is

$$\vec{v}^* = \frac{\vec{v}_m R_m^3 + \vec{v}_n R_n^3}{(R^*)^3}. \qquad (28)$$

Similarly, the bubble position is weighted by each bubble's volume at the moment of coalescence to obtain

$$\vec{Y}^* = \frac{\vec{Y}_m R_m^3 + \vec{Y}_n R_n^3}{(R^*)^3}. \qquad (29)$$

After these terms have been updated, the collision list is updated and the simulation advances as normal.

6. Model validation

Colin et al. (1991) performed experiments of bubble coalescence in a turbulent pipe flow in both normal and microgravity ($\vec{g} \approx 0$) conditions. The microgravity experiments were performed on an aircraft that flew a parabolic trajectory to obtain microgravity conditions for ~ 20–30 s for each experiment. The experimental setup composed of a long plexiglass tube, with a 4 cm diameter and length of 317 cm, broken into five sections. The central part of the pipe was $L_1 = 200$ cm $= 50D$ long, with visualizing test sections on both ends of the central section. The visualizing test sections were each $L_2 = 40.5$ cm $= 10.25D$ long. Void fraction probes were located near the ends of the pipe. Gas was injected and mixed with the fluid phase through a Venturi mixer at the inflow section. For low gas flow-rates and high fluid velocities, dispersed bubbles with a diameter on the order of a few millimeters were observed. As the bubbles traveled downstream, the bubbles grew larger due to coalescence. The void fraction of the microgravity experiment was 4.6% based on the empirical relation determined by Colin et al. (1991) of $U_G = 1.2U_m$, where the gas velocity $U_G = U_{GS}/\epsilon$ and ϵ is the average void fraction and U_{GS} is the superficial gas flow rate. The bulk Reynolds number, based on the mixture velocity, $U_m = U_{GS} + U_{LS}$, pipe diameter D and liquid viscosity ν_f, was 32,000. The Reynolds number based on the viscous scale velocity $u_\tau(\text{Re}_\tau \equiv D u_\tau/\nu_f)$ is equal to 1750 in the microgravity experiment. Our simulation was performed at conditions similar to the Colin et al. (1991) experiment with a superficial gas flow rate (U_{GS}) of 0.05 m/s and a bulk liquid flow speed (U_{LS}) of 0.85 m/s in microgravity.

The simulation parameters were chosen to be similar to experimental conditions by matching the inflow size distribution of bubbles, average void fraction and domain length. The simulation domain consists of a pipe with diameter D and length $L = 81D$, similar in length and Reynolds number as the Colin et al. (1991) experiment, whose length from the beginning of the first measurement section to the end of the last measurement section is $2L_2 + L_1 \approx 70D$. Bubbles were injected at the inflow plane, traveling downstream with the flow until exiting at the outflow plane. The simulation inflow corresponds with the inflow of the first visualization section in the experiment and the simulation outflow extends $11D$ beyond the outflow of the outflow experimental visualization section.
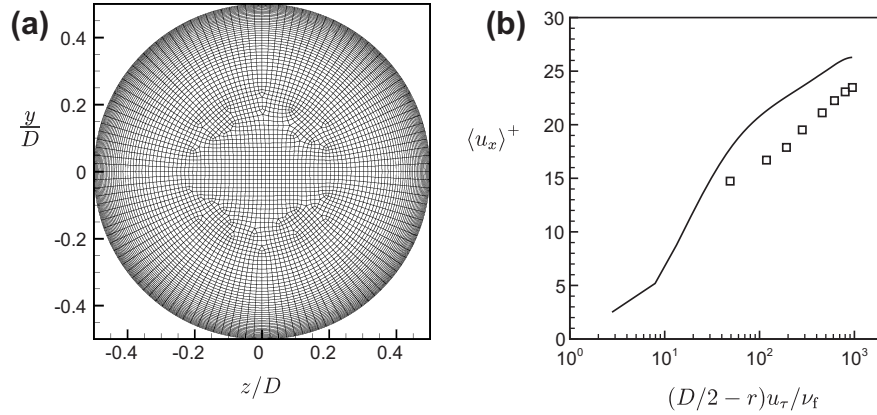
Fig. 3. (a) Cross-sectional mesh of turbulent pipe. (b) Time-averaged, streamwise, carrier fluid velocity as a function of distance from the wall, as compared to experiment. —, LES; □, Lawn (1971).

Table 1
Simulation and experimental (Colin et al., 1991) parameters.

Case	L	Re_τ	$\bar{g}$	ϵ	$\bar{d}$ (inflow)	$\bar{d}$ (outflow)
Colin et al. (1991)	70D	1750	0	0.046	0.062D	0.136D
LES	81D	1920	0	0.046	0.062D	0.146D

However, since the Colin et al. (1991) experiment did not provide details of the turbulent flow, a simulation of turbulent pipe flow with $Re_\tau = 1920$ was performed to validate mean flow and turbulent statistics with the experiment by Lawn (1971). In the simulation, $U_{ref} = 2u_\tau$ and a body force (κ) of $\kappa D/(\rho_f u_\tau^2) = 4$ was applied to counterbalance the shear stress as the wall of the $Re_\tau = 1920$ pipe flow. Periodic boundary conditions were applied in the streamwise direction for the carrier fluid. The bubbles feel the effect of κ through the inclusion of the Du_i/Dt term of Eq. (1) and therefore the body force does not need to be otherwise accounted for.

An unstructured mesh with 12.5×10^6 control volumes was used. The cross-sectional area of the pipe was discretized using an unstructured hexahedral mesh, with the circumference of the pipe discretized into 128 nodes (see Fig. 3a). In wall units, the azimuthal mesh spacing $D\Delta\theta^+/2 = 47$, where $r = \sqrt{y^2 + z^z}$ is the radial and θ is the azimuthal coordinate. Near the wall, a boundary layer with a minimum wall-normal spacing of $\Delta r/D = 0.002611$ was used and a boundary-layer mesh was grown for 34 rows from the pipe wall with a growth factor of 1.05. The minimum wall-normal spacing in wall units is 2.5. The cross-sectional mesh was extruded downstream with a uniform mesh in the streamwise direction. The grid spacing in the streamwise distance in wall units is $\Delta x^+ \equiv \Delta x u_\tau/\nu_f = 75.0$. The minimum wall-normal spacing Δr_{min}^+ is about twice that of the LES simulation with van-Driest wall-damping performed by Rudman and Blackburn (1999), though the azimuthal and streamwise mesh spacings are equal. A constant timestep of $\Delta t^+ = \Delta t \, u_\tau/D = 5 \times 10^{-5}$ was used. The timestep is smaller than that used in the DNS of turbulent pipe ($Re_\tau = 360$) by Eggels et al. (1994). The bubble timestep is $\Delta t_b = \Delta t/100$, as determined a posteriori though trial and error to obtain numerical stability.

The bubbles were injected in a random position within the inner 0.8D of the pipe cross-section, located at a streamwise distance of $x/D = 0.01$, and are injected with a constant volume-flux $\dot{\mathcal{V}}$. The bubble velocity is initialized to the local fluid velocity. The volume-flux of $N_{\Delta T}$ bubbles over timescale ΔT is obtained from

$$\dot{\mathcal{V}}_{\Delta T} = \frac{4\pi}{3\Delta T} \sum_{i=1}^{N_{\Delta T}} R_i^3. \tag{30}$$

The timescale ΔT can be broken into n equal parts of the carrier-fluid timestep Δt (i.e. $\Delta T = n\Delta t$). In these simulations, n was chosen to be 240 so that $\dot{\mathcal{V}}_{\Delta T} \approx \dot{\mathcal{V}}$. The bubble radius R_{mean} is the mean bubble radius of the inflow size distribution. The number of bubbles with size R_{mean} that it takes to obtain the volume-flux rate is

$$N_{mean} = \frac{3}{4} \frac{\dot{\mathcal{V}} \Delta T}{\pi R_{mean}^3}. \tag{31}$$

The probability of a bubble being injected into the flow during timestep Δt is obtained from

$$P_{inj} = \min\left(1, \frac{N_{mean}}{n}\right) \cdot \exp\left(-\frac{4\pi}{3\Delta t \, \dot{\mathcal{V}}} \sum_{i=1}^{N_{inj}} R_i^3\right), \tag{32}$$

where $0 \leqslant P_{inj} \leqslant 1$. Bubbles are injected until the probability P_{inj} is greater than that of a random number x_{ran}, with N_{inj} incremented with every bubble injected during timestep Δt. The random number x_{ran} is generated for each bubble injection and has a uniform distribution between 0 and 1.

The experimental (Colin et al., 1991) and simulation parameters are provided in Table 1. The mean bubble diameters ($\bar{d}$) were obtained from integration of the bubble size PDF at the inflow and outflow regions. The inflow size distribution in the simulation was taken directly from inflow distribution of the Colin et al. (1991) experiment. The bubble size at injection is sampled from the inflow size distribution using the rejection method. Once the bubbles are injected, coalescence is not allowed to occur until the bubbles reach a downstream distance of $x/D = 10$. This allows the bubbles to equilibrate in the flow after injection.

The length of the transitional inflow region (where coalescence is turned off while collisions are allowed) of $L_x = 10D$ was obtained through visual inspection of collision data for a *separate* simulation that was run with exactly the same numerical parameters as the simulation with coalescence, though coalescence was turned off. It was verified that the number of collisions N_c, probability of coalescence P_c (at moment of collision) and radial location of collision R_c were not changing with streamwise position by $L_x = 10D$, so it is assumed that the bubbles have achieved a position/velocity equilibrium within this region.

7. Results

7.1. Single-phase turbulence

Results for the carrier-phase turbulent flow in the bubbly-flow simulation are given in Fig. 3b and Fig. 4. Streamwise fluctuations are given by the variable u_x' and the wall-normal fluctuations are
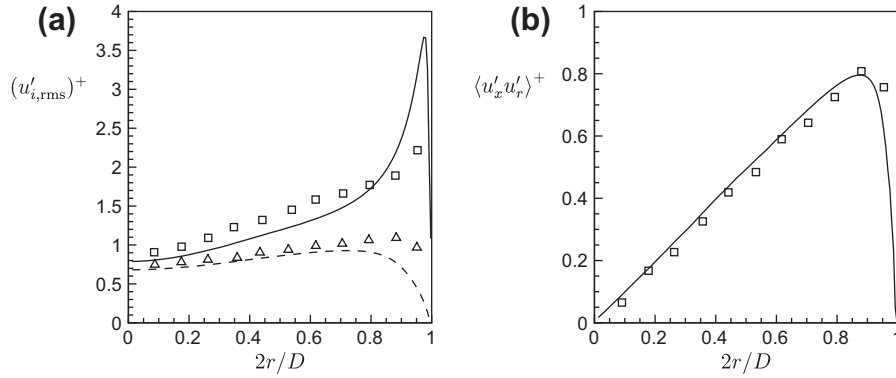
Fig. 4. Time-averaged turbulent fluctuations versus distance from the center of the pipe. (a) RMS fluctuations as compared to experiment. —, $(u'_{x,\mathrm{rms}})^+$ LES; – –, $(u'_{r,\mathrm{rms}})^+$ LES; $\square$, $(u'_{x,\mathrm{rms}})^+$ Lawn (1971); $\triangle$, $(u'_{r,\mathrm{rms}})^+$ Lawn (1971). (b) Reynolds shear stress. —, $\overline{u'_x u'_r}^+$ LES; $\square$, $\overline{u'_x u'_r}^+$ Lawn (1971).
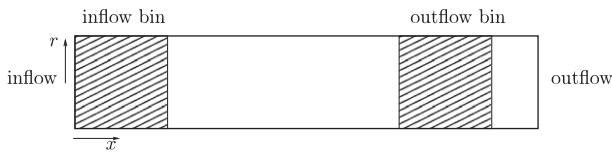
Fig. 5. Inflow and outflow bins for measurement of bubble properties. The length of the inflow/outflow bins is $L_2 = 10D$. The distance between the inflow and outflow bins is L_1. The total distance to the end of the last measurement section is $2L_2 + L_1 = 70D$.

Fig. 6. Streamwise bins for measurement of bubble properties. Each bin ($i = 1, 2, 3, \ldots$) samples data from bubbles that reside within its streamwise domain ($x_i - \Delta x_i/2 \leqslant x \leqslant x_i + \Delta x_i/2$).

given by u'_r. The data was averaged in the streamwise and the azimuthal directions. Single-phase statistics were averaged over 2.8 flow-through timescales (based on a mean velocity of $U_{\mathrm{bulk}}/(2u_\tau) = 11.2$ and a domain length of $81D$).

The simulation over-predicts the streamwise mean velocity, due to a lack of resolution near the wall. In a wall-bounded flow, the shear stress at the wall directly determines the mass flow rate for a given mean pressure gradient. Since the shear is under-resolved, the mass-flux though the pipe is increased to balance the reduced wall shear. This leads to over-predicting the mean streamwise velocity $\langle u_x \rangle$ and $u'_{x,\mathrm{rms}}$. Without near-wall models for LES, the over-prediction of $\langle u_x \rangle$ and $u'_{x,\mathrm{rms}}$ prediction is expected, though good agreement for the turbulence intensities is obtained for $u'_{x,\mathrm{rms}}$ and $u'_{r,\mathrm{rms}}$ away from the wall and $\overline{u'_x u'_r}$ in general when compared to results from Lawn (1971). No grid convergence studies have been performed. The simulation is of similar resolution of Rudman and Blackburn (1999), though our LES is performed without a wall-model. Due to the large Reynolds numbers ($\mathrm{Re}_\tau = 1920$) and large streamwise distance ($L/D = 81$), extreme computational resources would be required to completely resolve the flow, which is beyond the scope of this paper.

Even though the mean velocities are over-predicted near the pipe center, the turbulence intensities (which are mainly responsible for bubble–bubble collisions) are reasonable except very near the wall (where little collisions occur). With an over-prediction of the mean streamwise velocity, we expect the bubbles to be carried downstream more quickly than as observed in experiment, which will affect the streamwise dependence of the collision parameters. However, we do not expect the qualitative behavior to change due to the over-prediction of the mean velocity, which we deduce from the agreement of size-distribution between our simulation and experiment.

7.2. Effect of coalescence

In the simulation, bubble size distributions were obtained as a function of streamwise distance. The size distributions were aver-

aged over 3.9 flow-through timescales. The simulation domain was broken into 15 discrete, equally-sized sections in the streamwise direction, with a $\Delta x_{\mathrm{bin}} = 10D$. The first measurement bin begins from the inflow plane ($x = 0D$) and ends at $x/D = 10$. Corresponding with the experimental location (outflow measurement), the last measurement section samples bubble data from $60 \leqslant x/D \leqslant 70$. The inflow and outflow measurement sections are visualized in Fig. 5. Besides the inflow and outflow locations, measurement bins extended from the inflow plane to the outflow plane in the simulation, with a $\Delta x_i = \Delta x_{\mathrm{bin}} = 10D$ (see Fig. 6).
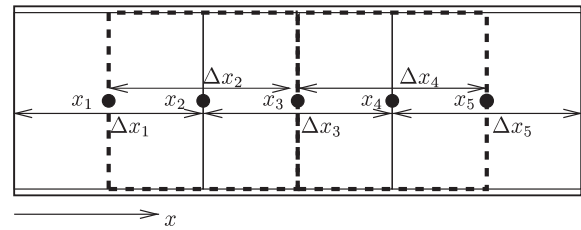
Fig. 7 plots the bubble size distribution of the LES simulation, along with the Colin et al. (1991) zero-g experiment at the inflow and outflow. Downstream of injection, the bubbles travel downstream with the flow and collide and coalesce with one another, causing the size distribution to shift towards larger sizes. The size distribution between the experiment and simulation show excellent agreement. Due to coalescence, the number density of the bubbles decreases as the bubbles travel downstream. This is observed in Fig. 8, which plots instantaneous position of bubbles in the pipe flow, both near and far downstream of bubble injection. Far downstream, much larger bubbles are observed than near injection and the overall number of bubbles has decreased.

8. Collision details

The evolution of the bubble size distribution depends on the nature of the bubble–bubble collisions. Bubble collision parameters such as relative velocity and bubble size determine the probability of coalescence. This section describes statistics of the bubble–bubble collision process. Mean quantities of collisions (such as $\overline{P_c}(x)$, $\overline{t_d/t_i}(x)$, etc., represented by $\bar{f}(x)$) are obtained by integrating over the PDF of f:

$$\bar{f}_j = \int_{-\infty}^{\infty} f \, \mathrm{PDF}(f) \, \mathrm{d}f, \tag{33}$$
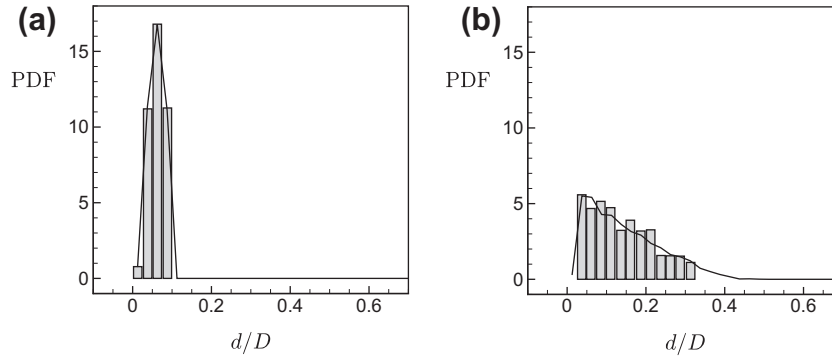
Fig. 7. Comparison of probability distribution function of bubble size from simulation to Colin et al. (1991) experiment. (a) Inflow distribution is sampled over $0 \leqslant x/D \leqslant 10$ and (b) outflow distribution is sampled over $60 \leqslant x/D \leqslant 70$. Solid lines represent simulation results and bars represent results from Colin et al. (1991).
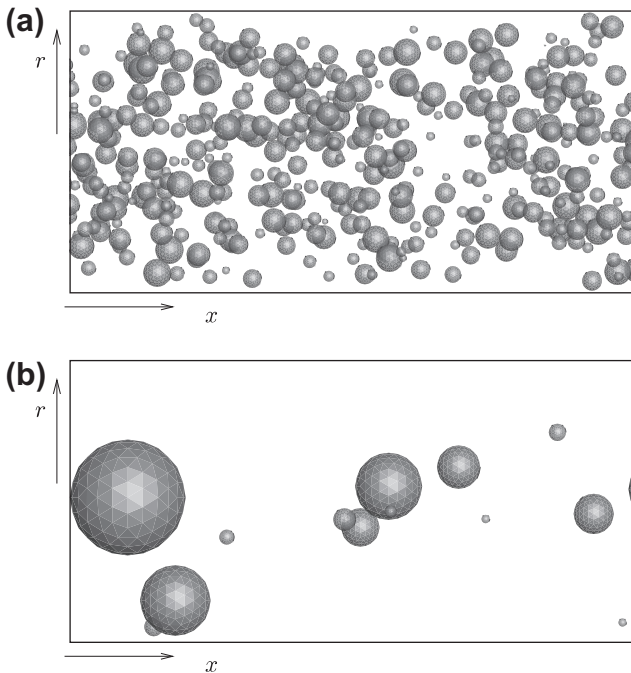

Fig. 8. Instantaneous position of bubbles in turbulent pipe flow, with coalescence. Bubbles are proportional to actual size. Flow is from left to right. View is looking through the pipe, perpendicular to the pipe flow, with the top and bottom boundaries of each figure at $r/D = 0.5$. (a) Near inflow ($4 \leqslant x/D \leqslant 6$). (b) Near outflow ($68 \leqslant x/D \leqslant 70$).

where the quantities f are sampled for bubbles located within the streamwise bin j between $x_j - \Delta x_{\text{bin}}/2 \leqslant x \leqslant x_j + \Delta x_{\text{bin}}/2$.

Instead of averaging over the entire size distribution, mean statistics $\bar{f}(x, d_m, d_n)$ can also be obtained as a function of bubble diameter d_m, d_n and streamwise distance x by

$$\bar{f}(x, d_m, d_n) = \frac{1}{N_c(x, d_m, d_n)} \sum_{i=1}^{N_c(x,d_m,d_n)} f_i(x, d_m, d_n), \tag{34}$$

where $N_c(x, d_m, d_n)$ is the total number of collisions at x with bubble diameters d_m and d_n. $\bar{f}(x, d_m, d_n)$ is discretized into streamwise measurement bins and equally-sized bins for d_m and d_n. The bin size is determined from the maximum measured bubble diameter d_{max} in the streamwise bins by $\Delta d_m = \Delta d_n = d_{\text{max}}/10$ for a total of 10×10 bins for each streamwise bin for $\bar{f}(x, d_m, d_n)$. Since there is no statistical difference between d_m and d_n, $\bar{f}(x, d_m, d_n)$ is enforced to be symmetric about $d_m = d_n$. Statistics are obtained from four streamwise locations. For smoothness of mean quantities, samples that are larger than $Re_{\text{eq}} = 8000$, $t_d/t_i = 10$ and $V_o = 15$ are discarded from calculations of $\bar{f}(x, d_m, d_n)$ as outliers from visual inspection of their respective PDFs. Also, mean values of $\bar{f}(x, d_m, d_n)$ are not shown if obtained from less than 125 collisions from from bins over streamwise distances $0 \leqslant x/D \leqslant 10$, $10 \leqslant x/D \leqslant 20$ and $20 \leqslant x/D \leqslant 30$, while mean values are not shown if less than 25 collisions are used to obtain statistics from $45 \leqslant x/D \leqslant 55$. The "blanking" criteria of collisions was determined by visual inspection of the plots. We attempted to strike a balance between statistic convergence and runtime, and chose our blanking criteria so that the curves looked smooth and regular as possible. For much of the domain, 125 collisions per bin was reasonable, but as the number of collisions decreased with downstream distance (see Fig. 9a) and the blanking
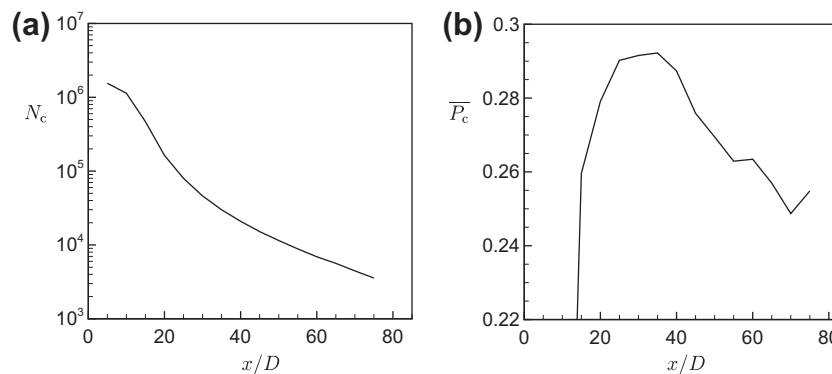
Fig. 9. (a) Streamwise evolution of total number of collisions N_c. (b) Streamwise evolution of mean probability of coalescence $\overline{P_c}$.
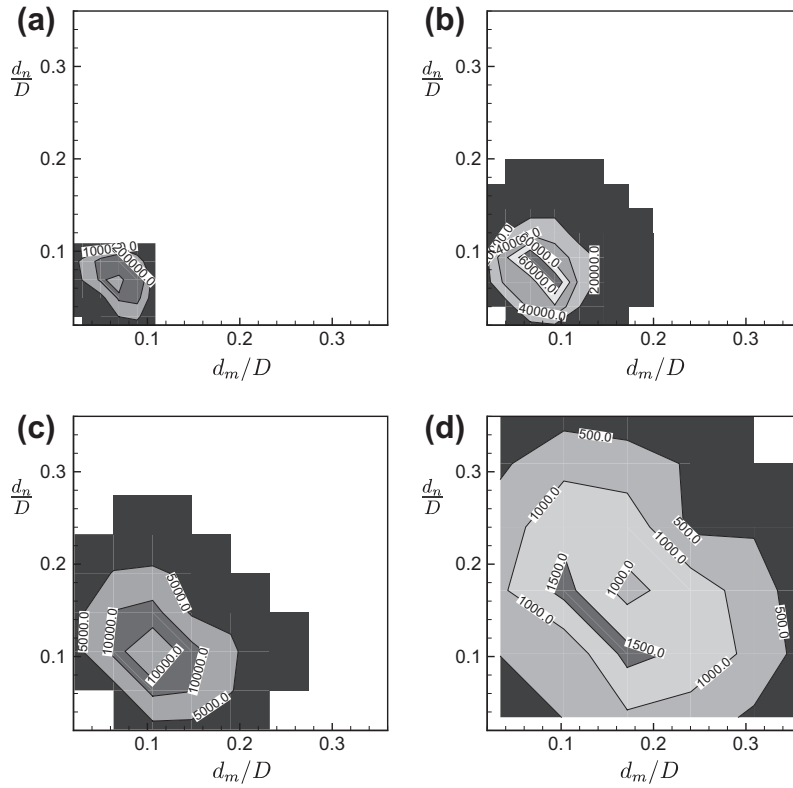
Fig. 10. Number of collisions $N_c(x, d_m, d_n)$ vs. d_m, d_n for (a) $0 \leqslant x/D \leqslant 10$, (b) $10 \leqslant x/D \leqslant 20$, (c) $20 \leqslant x/D \leqslant 30$, (d) $45 \leqslant x/D \leqslant 55$.
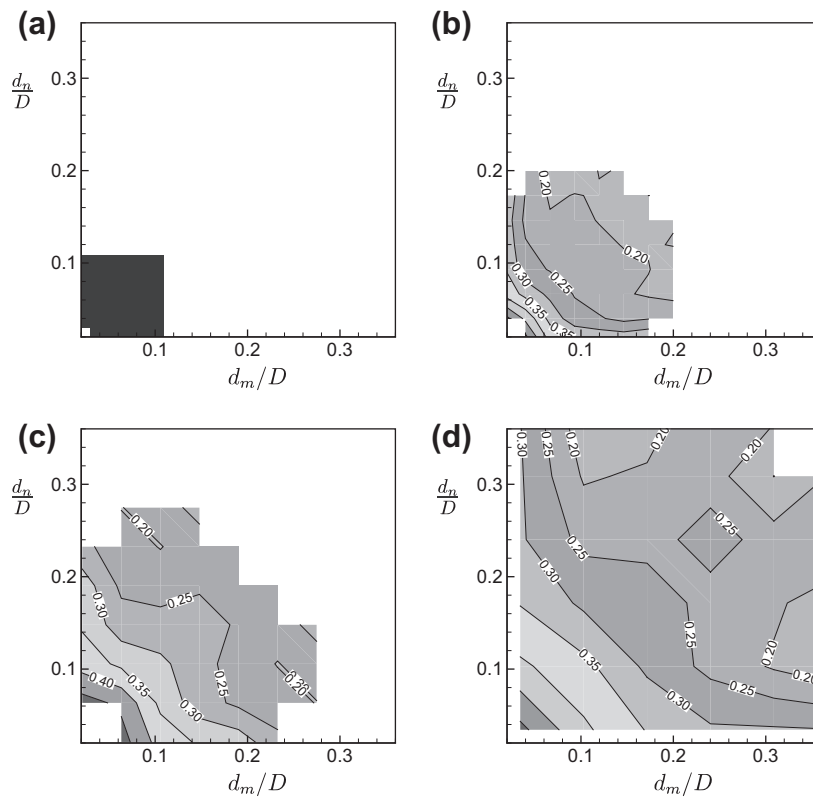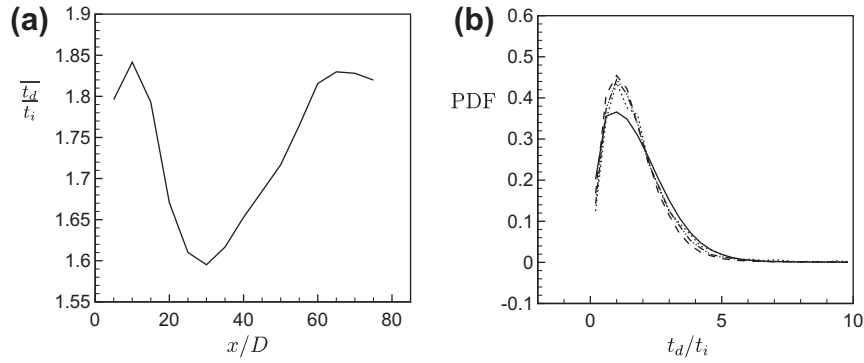

Fig. 11. Probability of coalescence $\overline{P}_c(x, d_m, d_n)$ vs. d_m, d_n for (a) $0 \leqslant x/D \leqslant 10$, (b) $10 \leqslant x/D \leqslant 20$, (c) $20 \leqslant x/D \leqslant 30$, (d) $45 \leqslant x/D \leqslant 55$.
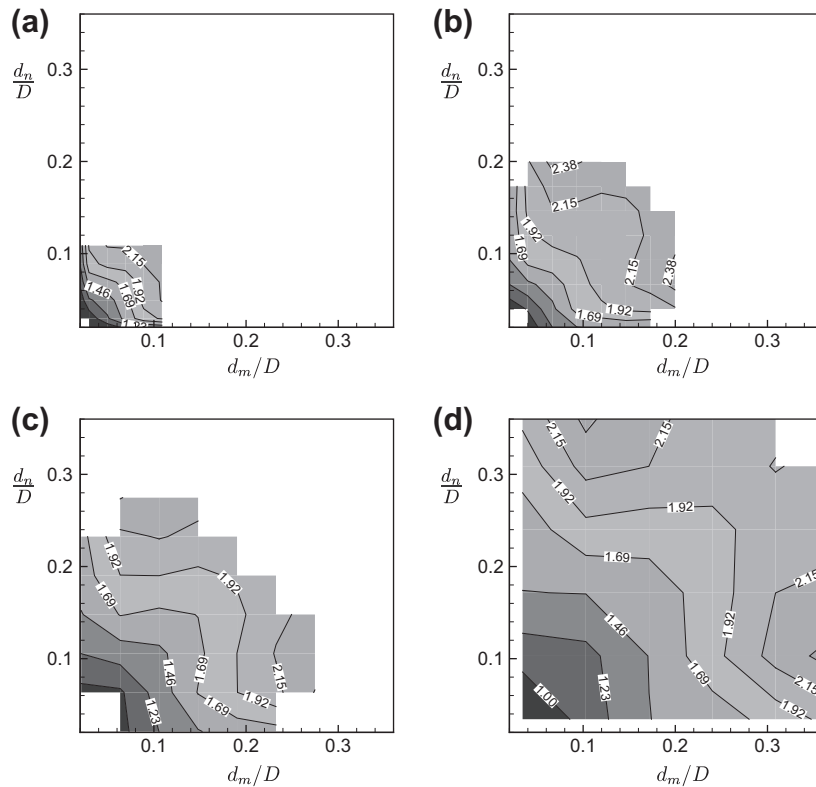
Fig. 12. (a) Streamwise evolution of $\overline{t_d/t_i}$. (b) PDF of t_d/t_i for four streamwise locations: —, $0 \leqslant x/D \leqslant 10$; – –, $20 \leqslant x/D \leqslant 30$; –·–·, $45 \leqslant x/D \leqslant 55$; ···, $70 \leqslant x/D \leqslant 80$.

criteria was reduced in order to view collision statistics without requiring extreme computational run-times.

Due to coalescence, the number of collisions $N_c(x)$ decreases rapidly with increasing distance as the number density of bubbles decreases (Fig. 9a). Fig. 10 plots the number of collisions observed as a function of streamwise distance and bubble size. The maximum number of collisions (for each streamwise bin) are observed for bubbles that are sized near the maximum of the PDF (d). With increasing downstream distance, N_c becomes more diffuse in (d_m, d_n) as the bubble size distribution also widens. The reduction of $N_c(x)$ makes obtaining converged statistics difficult far downstream ($x/D > 45$). As the size distribution increases due to coalescence, the location for maximum $N_c(x, d_m, d_n)$ moves to higher values of (d_m, d_n). The movement of the peak of $N_c(x, d_m, d_n)$ is consistent with the evolution of the size distribution, where larger bubbles are becoming more likely downstream due to coalescence and are also therefore more likely to collide with another bubble.

The mean probability of coalescence $\overline{P_c}(x)$ is plotted in Fig. 9b as a function of streamwise distance. The mean probability increases slightly near the inflow, then decreases with downstream distance. The value of $\overline{P_c} = 0$ from $0 \leqslant x/D \leqslant 10$ since coalescence is turned off in this region. The overall probability decreases from ~30% near the inflow to ~25% near the outflow. We do not have a physical explanation for the slight increase of $\overline{P_c}$ observed near the outflow. The most likely reason is a lack of statistical convergence due to the low number of collisions observed near the outflow, though the effect is not significant. The bubbles that collide far downstream are less likely to coalesce than bubbles that collide near the inflow. Fig. 11 plots the mean probability of coalescence $\overline{P_c}(x, d_m, d_n)$ as a function of x, d_m and d_n. A value of zero for Fig. 11a is due to coalescence not turned on in from $0 \leqslant x/D \leqslant 10$. Large bubbles are less likely to coalesce than small bubbles. The mean probability of coalescence is ~0.5 for small bubbles, and approaches 0.2 for large bubbles. With increasing downstream distance, P_c increases for constant bubble diameters (d_m, d_n).

Fig. 13. Ratio of coalescence timescales $\overline{t_d/t_i}(x, d_m, d_n)$ vs. d_m, d_n for (a) $0 \leqslant x/D \leqslant 10$, (b) $10 \leqslant x/D \leqslant 20$, (c) $20 \leqslant x/D \leqslant 30$, (d) $45 \leqslant x/D \leqslant 55$.
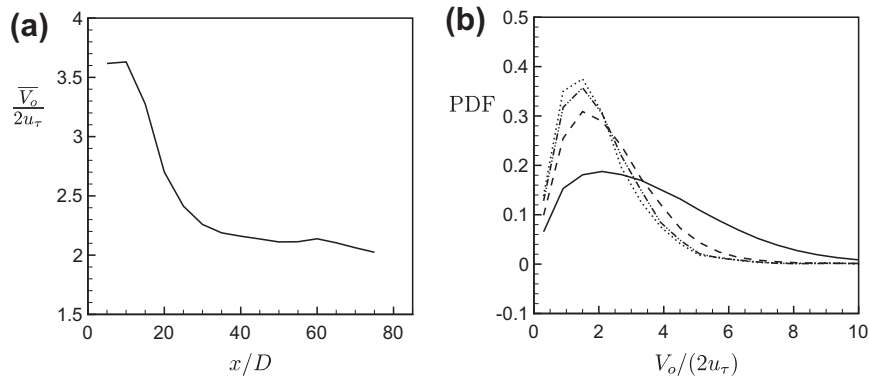
Fig. 14. (a) Streamwise evolution of the magnitude of the mean relative velocity $\overline{V_o}$ between colliding bubbles. (b) PDF of V_o for four streamwise locations: —, $0 \leqslant x/D \leqslant 10$; – –, $20 \leqslant x/D \leqslant 30$; –··–, $45 \leqslant x/D \leqslant 55$; ···, $70 \leqslant x/D \leqslant 80$.

The mean ratio of fluid drainage timescale to interaction timescale $\langle \overline{t_d/t_i}(x) \rangle$ slightly decreases then increases with downstream distance (see Fig. 12a), which correlates with the decrease of probability of coalescence $\overline{P}_c(x)$ with increasing downstream distance. Fig. 12b plots the PDF of t_d/t_i, and the PDFs of t_d/t_i are similar for the four streamwise locations shown. Small bubbles have smallest $\overline{t_d/t_i}(x, d_m, d_n)$, increasing with bubble size (at constant x) (see Fig. 13). With increasing downstream distance, $\overline{t_d/t_i}(x, d_m, d_n)$ decreases (for (d_m, d_n) held constant).

The mean relative velocity $\overline{V_o}(x)$ decreases with increasing downstream distance (Fig. 14a). Fig. 14b plots the evolution of the relative velocity PDF as a function of streamwise distance, with the distribution becoming more concentrated about the mode with increasing downstream distance. The mean relative velocity at collision $\overline{V_o}(x, d_m, d_n)$ is less for small bubbles as compared to large

bubbles (Fig. 15). For a constant (d_m, d_n), $\overline{V_o}(x, d_m, d_n)$ decreases with downstream distance. For constant x, $\overline{V_o}(x, d_m, d_n)$ increases with increasing (d_m, d_n).

The average collision Reynolds number $\overline{Re}_{eq}(x)$ is plotted in Fig. 16a as a function of streamwise distance. $\overline{Re}_{eq}(x)$ is ~1000 near the inflow, and increases with downstream distance. The PDF of Re_{eq} as a function of streamwise distance is given in Fig. 16b, with $Re_{eq} \sim 750$ the most probable value, though the PDF shifts towards larger values of collision Reynolds number with increasing streamwise distance. Mean collision Reynolds number $\overline{Re}_{eq}(x, d_m, d_n)$ increases with increasing bubble size (d_m, d_n) (Fig. 17). Small bubbles have the smallest $\overline{Re}_{eq}(x, d_m, d_n)$ for a given x. As downstream distance increases, the collision Reynolds number increases for constant bubble diameter. The results show that viscous effects on collision are small (large Re_{eq}).
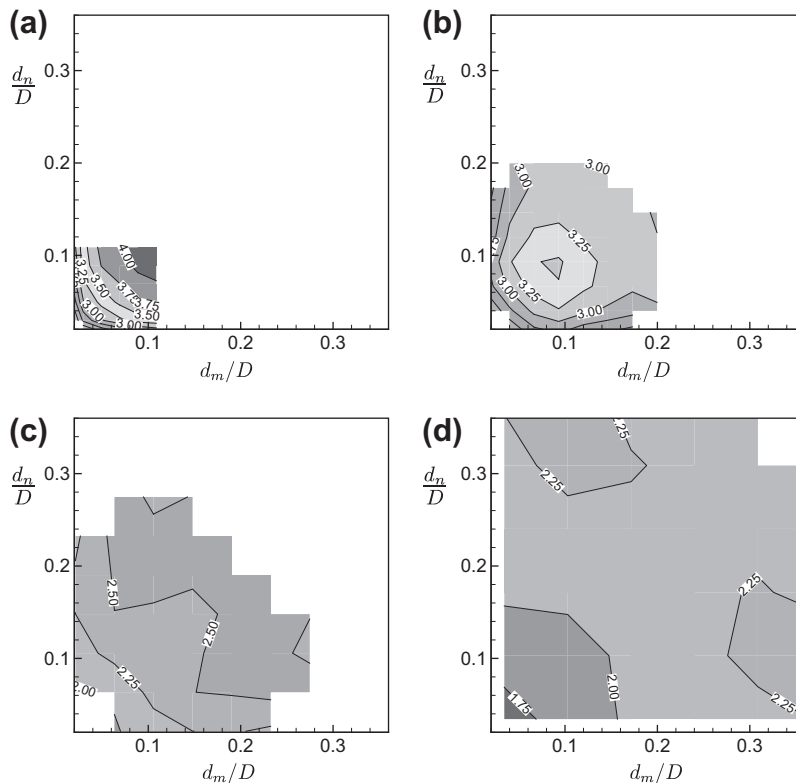
Fig. 15. Relative velocity of collision $\overline{V_o}(x, d_m, d_n)$ vs. d_m, d_n for (a) $0 \leqslant x/D \leqslant 10$, (b) $10 \leqslant x/D \leqslant 20$, (c) $20 \leqslant x/D \leqslant 30$, (d) $45 \leqslant x/D \leqslant 55$.
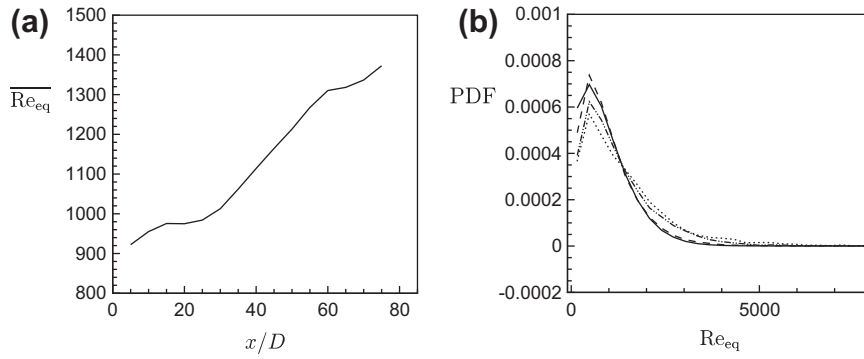
Fig. 16. (a) Streamwise evolution of $\overline{Re_{eq}}$. (b) PDF of Re_{eq} for four streamwise locations: —, $0 \leqslant x/D \leqslant 10$; − −, $20 \leqslant x/D \leqslant 30$; −·−·, $45 \leqslant x/D \leqslant 55$; ···, $70 \leqslant x/D \leqslant 80$.
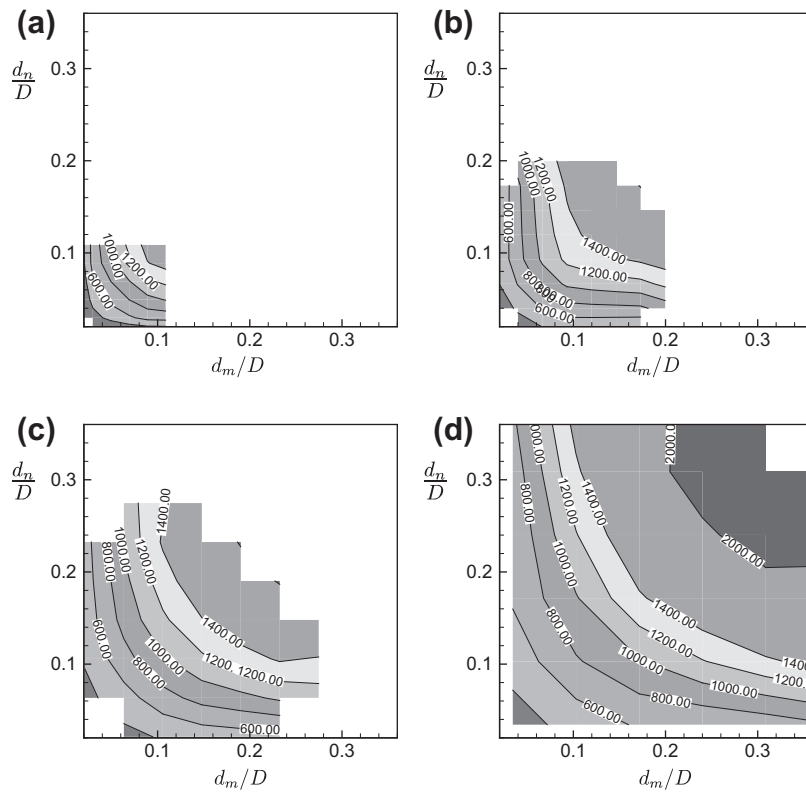

Fig. 17. Collision Reynolds number $\overline{Re}_{eq}(x, d_m, d_n)$ vs. d_m, d_n for (a) $0 \leqslant x/D \leqslant 10$, (b) $10 \leqslant x/D \leqslant 20$, (c) $20 \leqslant x/D \leqslant 30$, (d) $45 \leqslant x/D \leqslant 55$.
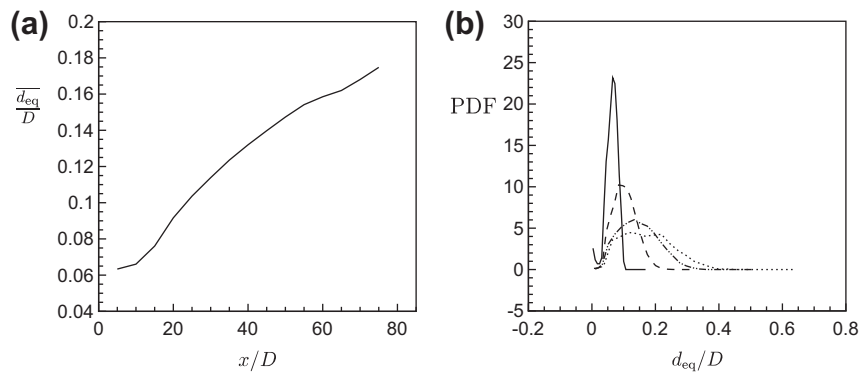

Fig. 18. (a) Streamwise evolution of $\overline{d_{eq}}$. (b) PDF of d_{eq} for four streamwise locations: —, $0 \leqslant x/D \leqslant 10$; − −, $20 \leqslant x/D \leqslant 30$; −·−·, $45 \leqslant x/D \leqslant 55$; ···, $70 \leqslant x/D \leqslant 80$.
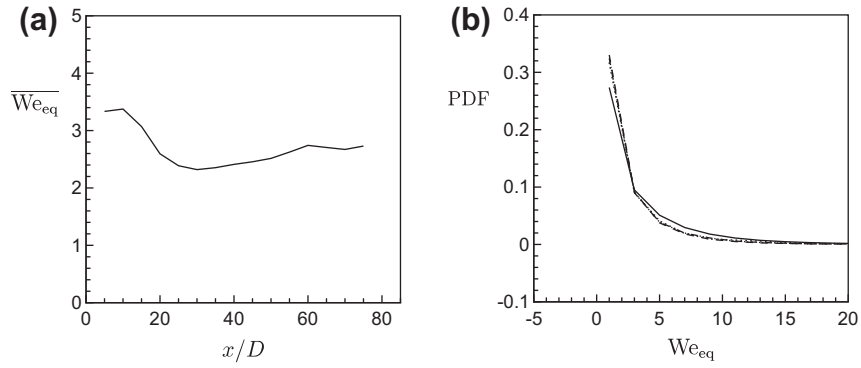
Fig. 19. (a) Streamwise evolution of $\overline{We_{eq}}$. (b) PDF of We_{eq} for four streamwise locations: —, $0 \leqslant x/D \leqslant 10$; – –, $20 \leqslant x/D \leqslant 30$; –··–, $45 \leqslant x/D \leqslant 55$; ···, $70 \leqslant x/D \leqslant 80$.
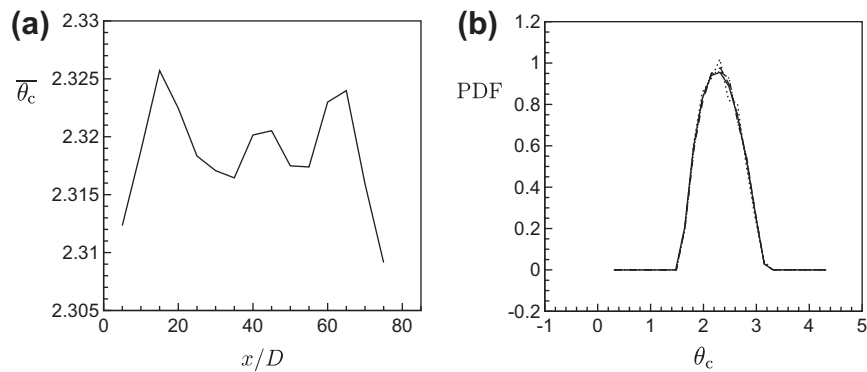

Fig. 20. (a) Streamwise evolution of $\overline{\theta_c}$ (θ_c is in radians). (b) PDF of θ_c for four streamwise locations: —, $0 \leqslant x/D \leqslant 10$; – –, $20 \leqslant x/D \leqslant 30$; –··–, $45 \leqslant x/D \leqslant 55$; ···, $70 \leqslant x/D \leqslant 80$.
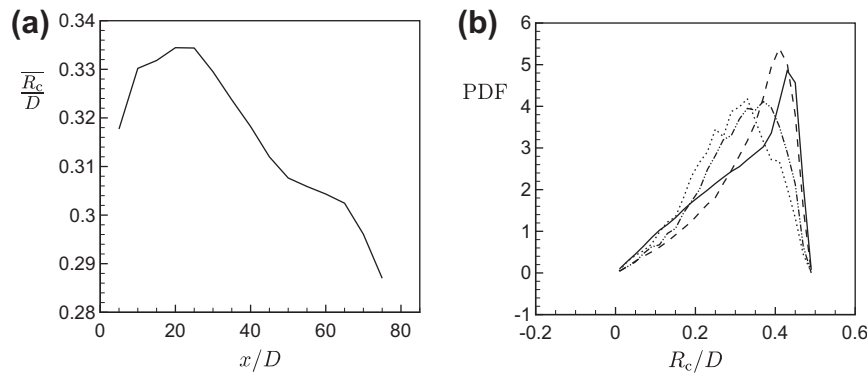

Fig. 21. (a) Streamwise evolution of $\overline{R_c}$. (b) PDF of R_c for four streamwise locations: —, $0 \leqslant x/D \leqslant 10$; – –, $20 \leqslant x/D \leqslant 30$; –··–, $45 \leqslant x/D \leqslant 55$; ···, $70 \leqslant x/D \leqslant 80$.

The average bubble size increases with downstream distance, as shown in Fig. 18a. Recall that $d_{eq} = (2d_m d_n)/(d_m + d_n)$. As the overall bubble size increase, so does d_{eq}. Also, the PDF of d_{eq} (Fig. 18b) becomes more weighted to larger bubbles as downstream distance increases due to coalescence. The mean collision Weber number $\overline{We_{eq}}(x)$ is ~3 (Fig. 19a), with the mean value slightly decreasing then increasing with downstream distance. In Fig. 19b, the PDFs of $We_{eq}(x)$ at four different streamwise locations are similar, with low Weber numbers being the most probable.

The mean collision angle $\theta_c(x)$ remains constant throughout the domain, with $\overline{\theta_c} = 2.33$ (in radians, see Fig. 20a), which is 135° from the line-of-centers of the colliding bubbles. Fig. 20b plots

the PDF of θ_c, and the PDFs are similar for the four streamwise locations shown. The mode of the collision angle θ_c is equal to the mean collision angle $\overline{\theta_c}$.

The mean radial location of collision, $\overline{R_c}(x)$, is obtained from the radial component (distance from the center of the pipe) of the point where the colliding bubbles m and n are touching. In Fig. 21a, $\overline{R_c}(x)$ decreases with increasing downstream distance, with collisions far downstream occuring more towards the center of the pipe. The PDF of R_c for four streamwise locations is shown in Fig. 21b. Since the collisions are turbulence driven, the most likely location for collision is near the wall, where turbulent fluctuations are largest. Turbulent fluctuations are lowest in the center of

the pipe, hence collisions near the center are not as likely to occur. With increasing downstream distance, the PDFs of R_c become more weighted to the center of the pipe.

9. Discussion

A one-way coupled Euler–Lagrangian methodology is used to simulate bubbly flow including the effect of coalescence, and bubble–bubble collisions are computed directly using a hard-sphere approach. A stochastic bubble coalescence model is developed, with the probability of coalescence determined from an expression of coalescence timescales derived by Kamp et al. (2001) for the Euler–Lagrangian approach, in which collisions and the relative velocity between colliding bubbles are computed directly.

Excellent agreement was obtained for the bubble size distribution between the Colin et al. (1991) experiment and numerical simulations including coalescence. Coalescence increases the mean size of the bubbles and also increases the prevalence of large bubbles in the flow. Bubble size increases through the merging of smaller bubbles, decreasing the number density of bubbles. Far downstream from injection, the total number of bubbles is greatly decreased which also decreases the overall number of collisions. The mean probability of coalescence $\overline{P_c}(x)$ was found to decrease slightly with increasing downstream distance which can be attributed to an increase in bubble size due to coalescence.

There is a large range of bubble sizes, thus fluid-dynamic effects can reduce the effective collision rate (impact efficiency smaller than unity) and influence the hydrodynamics forces on the bubbles. Turbulence has been shown to increase collision efficiency for heavy particles of very different or nearly equal size and vary as a function of turbulent dissipation rates (Wang et al., 2008). There exist models which allow consideration of impact efficiency (Ho and Sommerfeld, 2002, Wang et al. (2005)), although these effects are not accounted for in this approach. Additionally, it is clear that the largest bubbles have a diameter of $\approx 0.35D$ (see Fig. 7), which is much larger than the largest grid spacing ($\Delta x = 0.079D$). Therefore, the point-particle assumption is violated. The smallest bubbles are $\approx 0.01D$, which is larger than the smallest wall-normal spacing ($\Delta r = 0.002611D$) and smaller than the largest grid spacing. The bubble shape is also likely to differ from the assumed spherical shape, since the mean Weber number (based on bubble radius R, bubble relative velocity $|\vec{u} - \vec{v}|$ and surface tension coefficient σ) is ≈ 7 (averaged over all bubbles). The bubble shape has been shown to influence the drag and lift coefficients (Loth, 2008) which will influence instantaneous bubble behavior. In a point-particle approach, these affects cannot be directly accounted for; a full DNS including the bubble surfaces must be performed.

The direct effect of the subgrid stress (SGS) on the bubble transport has not been included. However, the particles *do feel* effects of the subgrid scales through the SGS model of the resolved flow. The direct effect of SGS is determined by the SGS time scales and energy content, and are small when the SGS time scale is large compared to bubble relaxation time and when the flow is nearly resolved. Others (Wang et al., 2009; Jin et al., 2010) have shown that the collision details are more sensitive to SGS than other first-order statistics (e.g. mean bubble path). Even without explicitly accounting for the effects of the SGS, the overall size distribution (Fig. 7) agrees quite well with experiment. This implies that the resolved unsteady flow was sufficient in reproducing the most important aspects of the flow, with respect to bubble collisions and coalescence.

The probability of coalescence is determined by an expression that is evaluated at the moment of collision and based on the ratio of fluid drainage and bubble-interaction timescales, where $P_c = \exp(-t_d/t_i)$. With an increase in the ratio of these timescales, the probability of coalescence decreases. There are a number of factors that influence the ratio of the coalescence timescales. Recall the expression (Eq. (23))

$$\frac{t_d}{t_i} \propto \sqrt{\frac{3\rho_f V_o^2 d_{eq}}{C_{vm}\sigma}}.$$

The only parameters that vary from collision-to-collision are V_o, d_{eq} and C_{vm}. From inspection of the equation for P_c it is evident that P_c decreases with downstream distance due to an increase in the ratio of coalescence timescales. Due to coalescence, d_{eq} increases as a function of $d_{eq} = (2d_m d_n)/(d_m + d_n)$. The coalescence timescale $t_d/t_i \propto \sqrt{d_{eq}}$, thus an increase in bubble diameter will also increase t_d/t_i, reducing the probability of coalescence at the moment of collision. Physically, this can be understood since it will take longer for surface tension to drain the fluid from between small bubbles than large bubbles. The coalescence timescale $t_d/t_i \propto \sqrt{1/C_{vm}}$, thus as the ratio of bubble diameters d_m/d_n departs from 1, the value of C_{vm} decreases. This increases the timescale t_d/t_i, reducing the probability of coalescence at the moment of collision. The effect can be seen in Fig. 11, where the probability of coalescence $\overline{P_c}(x, d_m, d_n)$ increases for bubbles with large ratios of relative bubble sizes. The relative velocity $V_o \propto t_d/t_i$, therefore as $\overline{V_o}(x)$ decreases with downstream distance, the effect is to reduce the probability of coalescence.

With increasing downstream distance, the radial location of bubble–bubble collision $\overline{R_c}(x)$ increases. This is due to the finite size of the large bubbles, who are not able be as near the wall as small bubbles. The velocity scales near the center of the pipe are much larger than that near the wall. Thus, bubbles colliding near the center of the pipe will also have a smaller relative velocity V_o since their velocities are more correlated. However, for a given streamwise location, the relative velocity is shown to increase with increasing bubble size (Fig. 15). Also, the drag coefficient of the large bubble will decrease (since Re_b increases) and the large bubble is less likely to follow the local flow than smaller bubbles. Other small bubbles in the nearby vicinity are likely to be more correlated to the flow (through a larger drag coefficient), thus small bubbles colliding will have a smaller relative velocity and are more likely to coalesce.

Acknowledgments

References

Allen, M.P., Tildesley, D.J., 1988. Computer Simulation of Liquids. Clarendon Press, New York.

Apte, S.V., Mahesh, K., Moin, P., Oefelein, J.C., 2003. Large-eddy simulation of swirling particle-laden flows in a coaxial-jet combustor. Int. J. Multiphase Flow 29, 1311–1331.

Auton, T.R., 1987. The lift force on a spherical body in a rotational flow. J. Fluid Mech. 183, 199–218.

Auton, T.R., Hunt, J.C.R., Prud'homme, M., 1988. The force exerted on a body in inviscid unsteady non-uniform rotational flow. J. Fluid Mech. 197, 241–257.

Batchelor, G.K., 1967. An Introduction to Fluid Dynamics. Cambridge University Press, Cambridge, UK.

Bokkers, G.A., Laverman, J.A., van Sint Annaland, M., Kuipers, J.A.M., 2006. Modelling of large-scale dense gas–solid bubbling fluidised beds using a novel discrete bubble model. Chem. Eng. Sci. 61, 5290–5302.

Chen, P., Sanyal, J., Duduković, M.P., 2005. Numerical simulation of bubble columns flows: effect of different breakup and coalescence closures. Chem. Eng. Sci. 60, 1085–1101.

Chesters, A.K., 1991. The modelling of coalescence processes in fluid-liquid dispersions – a review of current understanding. Trans. I. Chem. E. 69, 259–270.

Chesters, A.K., Hofman, G., 1982. Bubble coalescence in pure liquids. Appl. Sci. Res. 38, 353–361.

Colin, C., Fabre, J., Dukler, A.E., 1991. Gas–liquid flow at microgravity conditions – I. Dispersed bubble and slug flow. Int. J. Multiphase Flow 17, 533–544.

Coulaloglou, C.A., Tavlarides, L.L., 1977. Description of interaction processes in agitated liquid–liquid dispersions. Chem. Eng. Sci. 32, 1289–1297.

Darmana, D., Deen, N.G., Kuipers, J.A.M., 2006. Parallelization of an Euler–Lagrange model using mixed domain decomposition and a mirror domain technique: application to dispersed gas–liquid two-phase flow. J. Comput. Phys. 220, 216–248.

Duineveld, P.C., 1994. Bouncing and coalescence of two bubbles in water. Ph.D. thesis, University of Twente, The Netherlands.

Eggels, J.G.M., Unger, F., Weiss, M.H., Westerweel, J., Adrian, R.J., Friedrich, R., Nieuwstadt, F.T.M., 1994. Fully developed turbulent pipe flow: a comparison between direct numerical simulation and experiment. J. Fluid Mech. 268, 175–209.

Elghobashi, S., Truesdell, G.C., 1992. Direct simulation of particle dispersion in a decaying isotropic turbulence. J. Fluid Mech. 242, 655–700.

Fede, P., Simonin, O., 2006. Numerical study of the subgrid fluid turbulence effects on the statistics of heavy colliding particles. Phys. Fluids 18, 045103.

Germano, M., Piomelli, U., Moin, P., Cabot, W.H., 1991. A dynamic subgrid-scale eddy viscosity model. Phys. Fluids A 3, 1760–1765.

Haberman, W.L., Morton, R.K., 1953. An experimental investigation of the drag and shape of air bubbles rising in various liquids. David W. Taylor Model Basin Report 802.

Ho, C.A., Sommerfeld, M., 2002. Modelling of micro-particle agglomeration in turbulent flows. Chem. Eng. Sci. 57, 3073–3084.

Jin, G., He, G.-W., Wang, L.-P., 2010. Large-eddy simulation of turbulent collision of heavy particles in isotropic turbulence. Phys. Fluids 22, 055106.

Johnson Jr., V.E., Hsieh, T., 1966. The influence of the trajectories of gas nuclei on cavitation inception. In: 6th Naval Hydrodynamics Symposium, pp. 163–179.

Kamp, A.M., Chesters, A.K., Colin, C., Fabre, J., 2001. Bubble coalescence in turbulent flows: a mechanistic model for turbulence-induced coalescence applied to microgravity bubbly pipe flow. Int. J. Multiphase Flow 27, 1363–1396.

Lamb, H., 1945. Hydrodynamics, sixth ed. Dover Publications, New York.

Lawn, C.J., 1971. The determination of the rate of dissipation in turbulent pipe flow. J. Fluid Mech. 48, 477–505.

Legendre, D., Magnaudet, J., 1998. The lift force on a spherical bubble in a viscous linear shear flow. J. Fluid Mech. 368, 81–126.

Lilly, D.K., 1992. A proposed modification of the Germano subgrid-scale closure method. Phys. Fluids A 4, 633–635.

Loth, E., 2008. Quasi-steady shape and drag of deformable bubbles and drops. Int. J. Multiphase Flow 34, 523–546.

Mahesh, K., Constantinescu, G., Moin, P., 2004. A numerical method for large-eddy simulation in complex geometries. J. Comput. Phys. 197, 215–240.

Mattson, M., Mahesh, K., 2011. Simulation of bubble migration in a turbulent boundary layer. Phys. Fluids 23, 045107.

Muppidi, S., Mahesh, K., 2008. Direct numerical simulation of passive scalar transport in transverse jets. J. Fluid Mech. 598, 335–360.

Olmos, E., Gentric, C., Vial, Ch., Wild, G., Midoux, N., 2001. Numerical simulation of multiphase flow in bubble column reactors. Influence of bubble coalescence and break-up. Chem. Eng. Sci. 56, 6359–6365.

Pozorski, J., Apte, S.V., 2009. Filtered particle tracking in isotropic turbulence and stochastic modeling of subgrid-scale dispersion. Int. J. Multiphase Flow 35, 118–128.

Prince, M.J., Blanch, H.W., 1990. Bubble coalescence and break-up in air-sparged bubble columns. A.I.Ch.E. J. 36, 1485–1499.

Rudman, M., Blackburn, H.M., 1999. Large eddy simulation of turbulent pipe flow. In: 2nd International Conference on CFD in Minerals and Process Industries. Melbourne, Australia, pp. 503–508.

Sangani, A.S., Didwania, A.K., 1993. Dynamic simulations of flows of bubbly liquids at large Reynolds numbers. J. Fluid Mech. 250, 307–337.

Sommerfeld, M., Bourloutski, E., Bröder, D., 2003. Euler/Lagrange calculations of bubbly flows with consideration of bubble coalescence. Can. J. Chem. Eng. 81, 508–518.

Sridhar, G., Katz, J., 1995. Drag and lift forces on microscopic bubbles entrained by a vortex. Phys. Fluids 7, 389–399.

Sundaram, S., Collins, L.R., 1997. Collision statistics in an isotropic particle-laden turbulent suspension. Part 1: direct numerical simulations. J. Fluid Mech. 335, 75–109.

Thomas, N.H., Auton, T.R., Sene, K., Hunt, J.C.R., 1984. Entrapment and transport of bubbles by plunging water. In: Brutsaert, W., Jirka, G.H. (Eds.), Gas Transfer at Water Surfaces. D. Reidel Publishing Co., pp. 255–268.

Trevorrow, M.V., Vagle, S., Farmer, D.M., 1994. Acoustical measurements of microbubbles within ship wakes. J. Acoust. Soc. Am. 95, 1922–1930.

van den Hengel, E.I.V., Deen, N.G., Kuipers, J.A.M., 2005. Application of coalescence and breakup models in a discrete bubble model for bubble columns. Ind. Eng. Chem. Res. 44, 5233–5245.

Wang, L.-P., Ayala, O., Kasprzak, S.E., Grabowski, W.W., 2005. Theoretical formulation of collision rate and collision efficiency of hydrodynamically interacting cloud droplets in turbulent atmosphere. J. Atmos. Sci. 62, 2433–2450.

Wang, L.-P., Ayala, O., Rosa, B., Grabowski, W.W., 2008. Turbulent collision efficiency of heavy particles relevant to cloud droplets. New J. Phys. 10, 075013.

Wang, L.-P., Rosa, B., Gao, H., He, G., Jin, G., 2009. Turbulent collision of inertial particles: point-particle based, hybrid simulations and beyond. Int. J. Multiphase Flow 35, 854–867.